Application of an Inverse Design Methodology to Rotor Tip Design

Michelle Ku, Georgia Institute of Technology, Atlanta, GA, USA
Aishwerya Gahlot, Georgia Institute of Technology, Atlanta, GA, USA
Lakshmi N. Sankar, Georgia Institute of Technology, Atlanta, GA, USA

Abstract

An inverse design technique is described for improving the aerodynamic characteristics of 2-D rotor sections and helicopter rotor blade tip regions. This methodology requires the specification of a target pressure distribution that achieves the design lift coefficient, while reducing the profile drag by delaying transition to turbulent flow and mitigating boundary layer growth by reducing the adverse pressure gradients wherever possible. The peak local Mach numbers are also kept low enough to delay the formation of shock waves and the attendant wave drag and shock noise. This methodology is independent of the flow solver used to predict the surface pressure data over the intermediate geometries during the design iterations, allowing a variety of flow solvers to be used. Sample 2-D applications are shown for 2-D airfoil design where the present methodology is used with an in-house panel method which is used to generate the surface pressures. This methodology is subsequently applied to the redesign of the S76 rotor tip region for improved performance at high thrust settings.

1. INTRODUCTION

Over the past several decades, considerable progress has been made on the modeling and design of rotor blades for conventional helicopters, as well as eVTOL and UAS systems. For example, Johnson and his coworkers have developed a series of lifting rotor and propeller analyses and accompanying design tools [1-3]. These tools have been successfully applied to a broad class of current and future generation civilian rotorcraft and eVTOL concepts [4-7]. In most of these approaches, a multidisciplinary approach is used, with the properties of the rotor blade (twist, taper, sweep, anhedral, and airfoils) as design variables. An optimization strategy is often used, where a combination of design objectives (low power consumption in hover and vibration, low noise, and low hub-load vibration levels) is achieved [8]. In these approaches, the family of airfoils are chosen a priori, or included in the design process using a genetic algorithm that combines the best features of existing airfoils over multiple evolutions.

In practice, the rotor tip operates in a highly three-dimensional flow environment. A 2-D airfoil that has a desirable laminar drag bucket behavior may perform poorly near the tip due to the cross flow induced by the tip vortex formation, presence of weak shock waves, and secondary trailing vortices that are generated in regions where the planform is discontinuous. The tip region of the rotor produces a major portion of the desired thrust and consumes a significant fraction of the available power. It is therefore desirable to reshape the blade contour in these regions to improve the rotor performance. Conventional 2-D airfoil design tools would not be suitable in such 3-D flow environments. An experienced designer would examine the surface pressure distribution of a given design and try to modify the 3-D pressure distribution that improves the rotor performance, using changes to the geometry guided by intuition and experience. Robust, user friendly, highly automated tools that guide the designer in this process are desirable. This work describes such an approach.

2. DESCRIPTION OF THE INVERSE DESIGN METHODOLOGY

The inverse design methodology used in this work is an extension of the technique proposed by Garabedian and McFadden [9] and applied to transonic wing design using a flow solver called

FLO22 [10]. This approach has been modified by the present authors for a variety of 2-D and 3-D applications [11-13].

The present inverse design approach iteratively modifies the rotor surface Z(x,r), where x represents the chordwise location of a surface point on the section and r represents the radial (or spanwise) location. The objective of the iterative process is to drive the surface pressure coefficient Cp(x,r) at any point on the surface, computed using any convenient flow analysis (CFD or panel method, as applicable) towards a target pressure coefficient Cp,target(x,r) specified by the user by changing the ordinate Z(x,r) by a small amount ΔZ(x,r) at each iteration.

Since the surface pressure distribution is influenced by the surface ordinate, its slope, and its curvature (or second derivative), the following heuristic equation is solved.

$$A(\Delta Z) + B\frac{\big(\partial(\Delta Z)\big)}{\partial\xi} - C\frac{\partial^2(\Delta Z)}{\partial\xi^2} = Cp(x,r) - Cp,target(x,r) \tag{1}$$

In the above equation, ξ is the square root of the non-dimensional distance along the chord line measured from the leading edge:

$$\xi = \sqrt{\frac{\mathrm{x}}{\mathrm{c}}}$$

Here the c is the local chord, and the three constants A, B, C are user-specified and drive the changes in the surface shape ΔZ to zero as the computed surface pressure distribution approaches the target values. A large value of the coefficients A, B, and C would cause the surface to change very slowly between iterations, while smaller values will cause larger changes and possibly lead to divergence of the iterative process.

In this approach, it is not necessary to specify the target pressure distribution over the entire rotor section surface. In some regions, the existing surface pressure values may be deemed acceptable by the designer and considered equal to “target” values. The differences in the pressure coefficient ΔCp, equal to Cp(x,r) -Cp,target(x,r) is set to zero in those regions.

The first and second derivatives are discretized by the three points (i, i-1, i+1), giving rise to a set of linear algebraic equations at all points (x,r).

The first derivative is approximated using the current point ‘i’ and the downstream point ‘i+1’ as shown below:

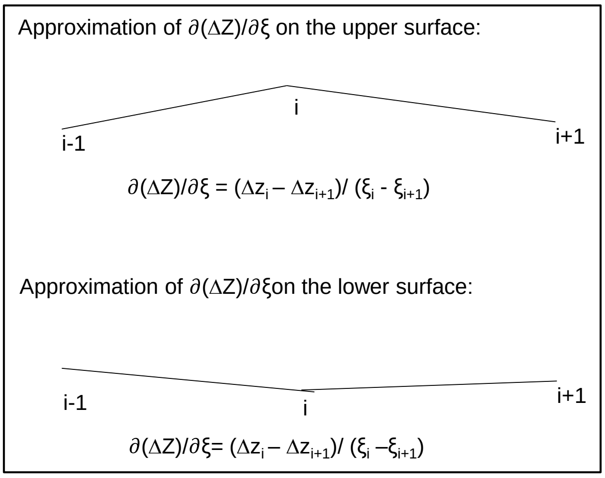

The second derivative at a point ‘i’ is related to the ΔZ values at adjacent points as shown below:

$$\frac{\partial^2(\Delta z)}{\partial\xi^2} = \frac{2}{\xi_{i+1} - \xi_{i-1}}\left[\frac{\Delta z_i - \Delta z_{i+1}}{\xi_i - \xi_{i+1}} - \frac{\Delta z_i - \Delta z_{i-1}}{\xi_i - \xi_{i-1}}\right]$$

Use of these finite difference approximations in equation (1) leads to the following tridiagonal system on the upper and lower surfaces.

$$(UU)_i\Delta z_{i+1} + (DD)_i\Delta z_i + (LL)_i\Delta z_{i-1} = \left(\Delta C_p\right)_i$$

At the leading and trailing edges, ΔZ is set to zero to ensure a closed airfoil shape.

The resulting tridiagonal system may be solved for the change to the geometry at all nodes over the rotor section. The geometry is updated and a new flow solution Cp(x,r) is computed. The iterative process is repeated until the geometry stops changing.

3. SAMPLE 2-D DESIGN APPLICATIONS

Figure 1 shows a sample application where the target pressure distribution is specified for the known configuration, a NACA 2412 cambered airfoil at zero angle of attack, and a generic starting configuration (a NACA 0012 airfoil). The intermediate airfoil shapes are iteratively changed until the expected target pressure distribution is achieved, typically in just 10 iterations, requiring less than one second on a desktop personal computer system. In this application, an inhouse 2-D panel method [14, 15] was used to generate the target pressure distribution, as well as the intermediate surface pressure distribution Cp(x) at each iteration.

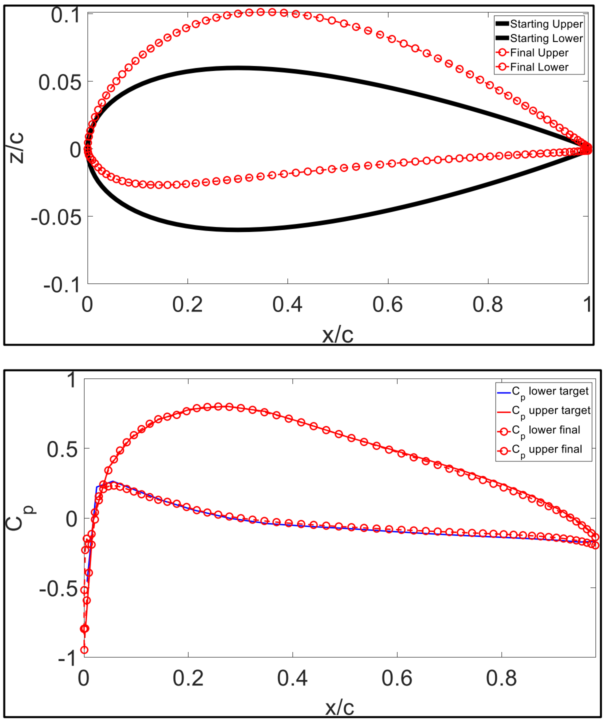

Figure 1: Application of 2-D Inverse Design Method to 2-D Airfoil Design (NACA 0012 Airfoil to NACA 2412 Airfoil)

A more interesting application would be to improve a well-known rotorcraft airfoil section such as the SC 1095 profile operating at a specified angle of attack, Mach number, and other parameters such as the Reynolds number. The designer would specify the desired target pressure values. Figure 2 shows the starting and target pressure distributions, while Figure 3 shows the starting and final airfoil shapes.

The area inside the pressure distribution curves in Figure 2 was held fixed, achieving the same lift coefficient as the starting airfoil at the same angle of attack. It is seen that the target pressure distribution has a favorable pressure gradient (or a near zero pressure gradient) over much of the upper surface. It is well known that a strong adverse pressure gradient would create an inflection point in the boundary layer velocity profile, making it more prone to transition. Secondly, in both laminar and turbulent flows, adverse pressure gradients would cause the boundary layer to grow more rapidly, affecting the pressure recovery at the trailing edge and adversely impacting the profile drag.

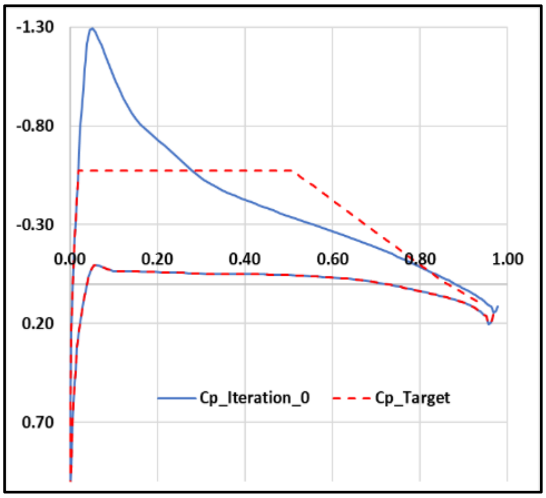

Figure 2: Starting and Target Pressure Distributions

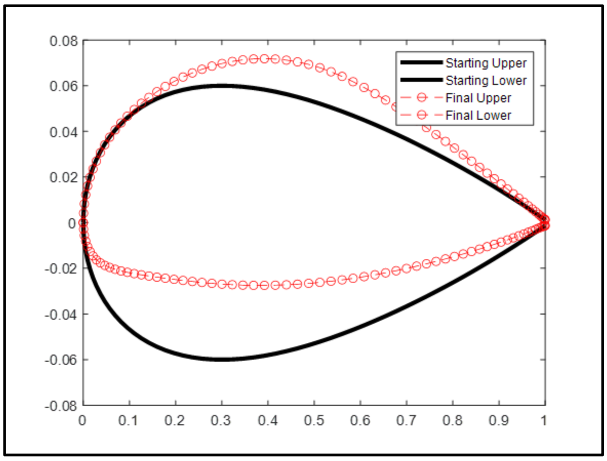

Figure 3: Starting SC 1095 and Final Airfoil Shapes

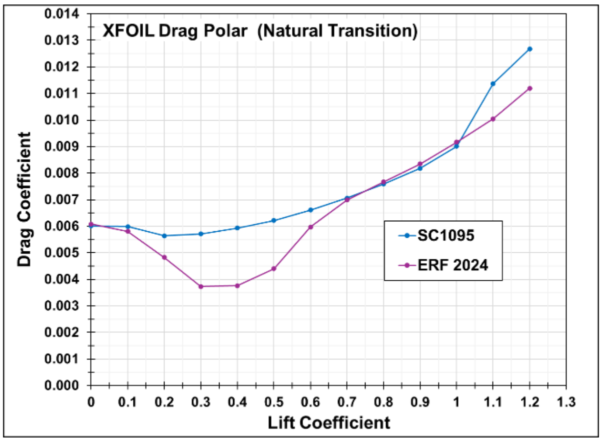

Figure 4a: Comparison of Drag Polars for SC 1095 Profile and the Redesigned Airfoil with Target Pressure Distribution Shown in Figure 2

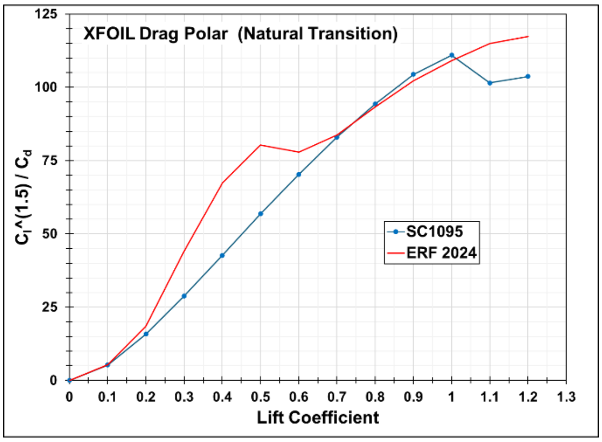

Figure 4b: Variation of $(C_l)^{3/2}/C_d$ vs. C_l for the Original and Redesigned Airfoil Sections

The final airfoil shape shown in Figure 3 was reanalyzed using XFOIL at a nominal Reynolds number of 3 million. The e^N transition, with N equal to 9, was used. Figure 4a shows the resulting drag polar for the SC 1095 airfoil and the new design. It is seen that the new airfoil generated using the present design process, has a desirable laminar drag bucket encompassing a broad range of lift coefficient values. The sectional pitching moment is found to be slightly higher than SC 1095, but acceptable.

Blade element theory suggests that the figure of merit of a rotor in hover can be maximized if the ratio $(C_l)^{3/2}$ / C_d is increased over a broad range of lift coefficients. Figure 5b indicates that for a broad range of lift coefficients between 0.2 and 0.7, the new airfoil has a significantly higher value of this quantity, indicating the suitability of the new airfoil in rotor design.

It is possible in the present approach to use other 2-D panel analyses, e.g. XFOIL, and extract the lift as well as drag characteristics of the initial geometry and the final design. It would only be necessary to generate a text file (within the design script) that creates an input file for XFOIL, with any starting airfoil (e.g. NACA 0012) and save the resulting surface pressure data for use in the inverse design process. The inverse design script would create a modified airfoil shape at each design iteration, which may be loaded into XFOIL.

4. APPLICATION TO S76 ROTOR TIP REDESIGN

In this application, the tip region of the S76 rotor blade is being redesigned to improve the hover performance on the rotor, especially at high thrust settings. This configuration was chosen because of the availability of the rotor geometry shape and hover test data in a well-documented form [16, 17].

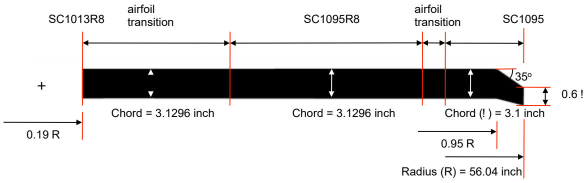

Figure 5: S76 Rotor Planform

Table 1. S-76 rotor properties

Radius, R	56.04 inches
Nominal chord, ĉ	3.1 inches
Equivalent chord, c_e	3.035 inches
Tip taper	60% ĉ
Root cutout	19% R
Sweep (leading-edge)	degrees at 95% R
Solidity	0.07043
Airfoils	SC1013R8, SC1095R8, SC1095
Number of blades, N_b	4

The flow solver used in this study is a hybrid Navier-Stokes/free-wake methodology called GT-Hybrid. This is a finite volume based three-dimensional unsteady viscous compressible flow solver which computes a Navier-Stokes solution only in the immediate vicinity of the rotor blades. Away from the rotor blades, the vortex wake is captured using a Lagrangian approach. This hybrid approach allows for an accurate and economical modeling of viscous features near the blades, and a “non-diffusive” modeling of the trailing wake in the far field. Ref. 19-21 show recent applications of this solver to the S76 rotor with and without anhedral effects. A one-equation Spalart-Allmaras model, with an algebraic transition model that turns off the turbulent kinetic energy production term in the laminar regions has been used [20-21].

Figure 6 below shows the variation of thrust and torque coefficients with pitch setting, at a tip Mach number of 0.65. Reasonable agreement with test data is observed. It should be noted that these simulations have been previously published in Ref. 21 and Ref. 22.

The major steps in the rotor tip redesign in the present approach are as follows:

1. A starting configuration (S76 in the present context) is chosen. This configuration is analyzed to determine the performance characteristics using a CFD tool such as GT-hybrid.

2. A particular thrust setting based on operating conditions (pressure altitude, density, temperature) of most interest to the operators is chosen.

3. The surface pressure coefficients at this setting at selected radial locations are chosen. In this study, the radial location of 90% has been chosen.

4. Target pressure distributions are specified at these locations.

5. The section airfoil profile, local pitch angle that the chord line makes with the plane of rotation, and Mach number, and the target pressure distribution are supplied to the modified Garabedian-McFadden Method (MGM) design tool.

6. The supplied target pressure distribution is converted into an incompressible flow pressure distribution using the Prandtl-Glauert rule. The design tool uses a panel method (our in-house tool or XFOIL) in conjunction with the MGM tool to arrive at new airfoil shapes at the chosen radial locations.

7. The new rotor sections are used to loft a new blade shape. The new rotor is reanalyzed using the same CFD analysis used in step 1 above.

The starting condition for the present redesign exercise was arbitrarily chosen to be the thrust setting at 10 degree collective, with a CT/ σ equal to 0.0966 (which corresponds to a gross weight of 12565 pounds at standard sea level conditions. Figure 5 indicates that the last 10% of the S76 rotor employs the SC 1095 airfoil, which produces a surface pressure distribution with a suction peak very close to the leading edge, similar in shape to the starting Cp distribution in Figure 2. The computed pressure distribution at the 90% radial location was specified as the starting pressure distribution, with the SC 1095 airfoil as the starting configuration, at the sectional angle of attack and Mach number based on the operating condition at this pitch setting. A flat rooftop target pressure distribution, very similar in shape to the target Cp values shown in Figure 2, was specified, with the same integrated sectional lift coefficient as the baseline S76 at this radial location.

The starting and the target Cp values were converted into equivalent incompressible pressure distributions using Prandtl-Glauert rule. The airfoil section at 90% was redesigned using the in-house panel code, coupled to the MGM design tool described earlier. The new airfoil shape was subsequently used in the new "modified" rotor, at all stations outboard of 90% radius. The blade sections inboard of 90% were left unchanged. No other changes to the blade planform or twist distribution were made.

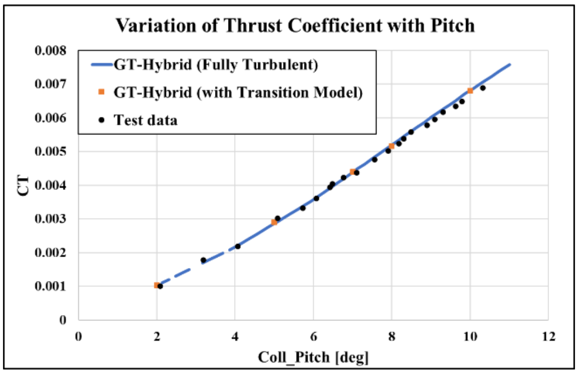

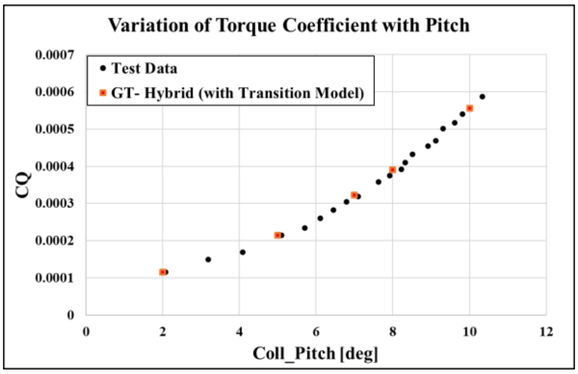

Figure 6: Comparison of Computed and Measured Thrust and Torque Variations with Collective Pitch for the S76 Rotor [21].

Figure 7 shows the integrated performance of the baseline S76 rotor, and the redesigned rotor for a range of thrust settings of interest. The data is also presented in tabular form for improved readability. At thrust settings CT/ σ below 0.08, the new rotor performs somewhat worse than the baseline S76. However, at higher thrust settings, the new rotor performs much better, reaching a peak figure of merit around 0.74 at a CT/σ of 0.126. In other words, for gross weights exceeding 10000 pounds at standard sea level conditions, the redesigned rotor would perform better than the baseline S76 rotor.

Coll_Pitch	CT	CT/Sigma	CP	CP/sigma	FM
2	0.00104	0.014764	0.000115425	0.001638864	0.20541
5	0.00290	0.041212	0.00021	0.003045017	0.51560
7	0.00439	0.062389	0.00032	0.00458524	0.63776
8	0.00517	0.073391	0.00039	0.005547982	0.67251
10	0.00680	0.09655	0.00056	0.007890104	0.71352
12	0.008584	0.12188	0.000786	0.011160017	0.71548

Figure 7a: S76 Baseline Rotor Performance

Coll_Pitch	CT	CT/Sigma	CP	CP/sigma	FM
6.0	0.00419	0.05951805	0.000313	0.004447	0.61273
8.0	0.00573	0.08135738	0.000445	0.0063183	0.68922
9.0	0.00654	0.09286367	0.000523	0.0074239	0.71532
9.4	0.00685	0.09730162	0.000556	0.0078938	0.72154
10.0	0.00730	0.10362441	0.000607	0.0086157	0.72655
12.0	0.00889	0.12623324	0.000800	0.0113621	0.74074

Figure 7b: Redesigned Rotor Performance

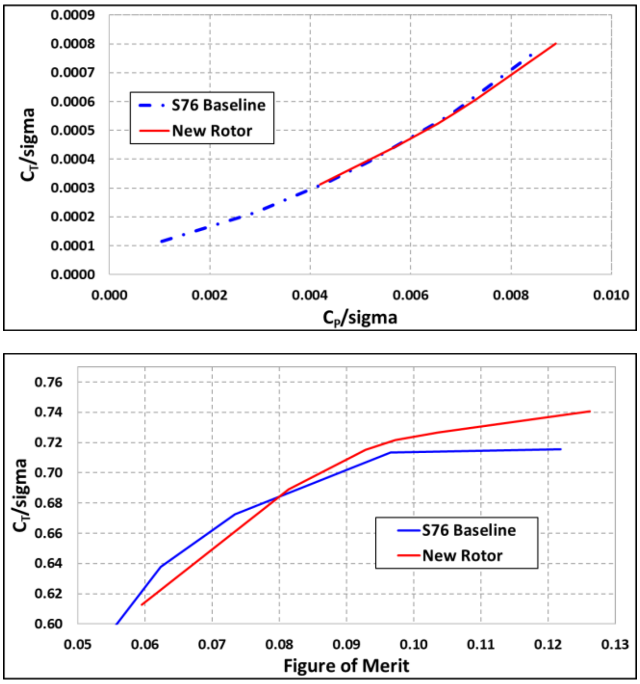

Figure 7c: Performance of S76 and Redesigned Rotors.

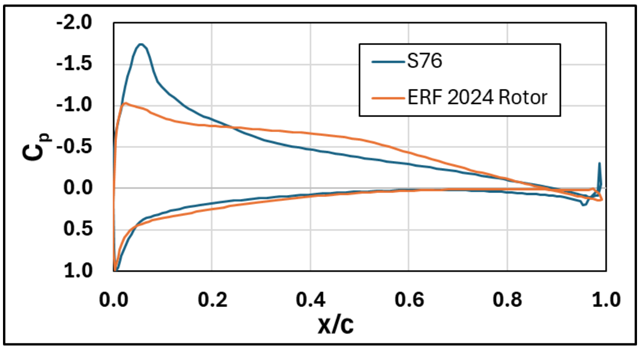

Figure 8: Comparison of the Surface Pressure Distribution at 90% R for the Two rotors at the same CT value of 0.0680

To gain a better understanding of the improved performance of the new rotor compared to the baseline S76 rotor, the surface pressure data at 90% radius for the two rotors at a thrust setting of 0.068 was plotted. Figure 8 shows the pressure distributions for the two rotors. It is seen that the new rotor has favorable or zero pressure gradient over much of the upper surface, compared to the S76 rotor. As stated earlier, the favorable pressure gradients would delay transition, and a lower growth rate of the boundary layer momentum thickness.

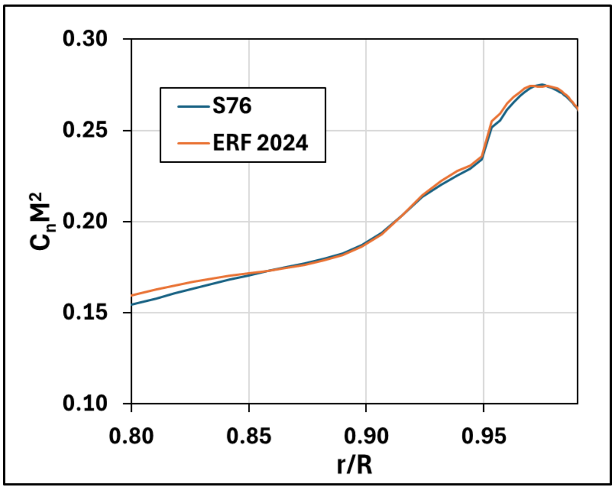

Figure 9: Radial variation of the Sectional Normal Force Coefficients C_nM^2 for the Two Rotors at 90% R

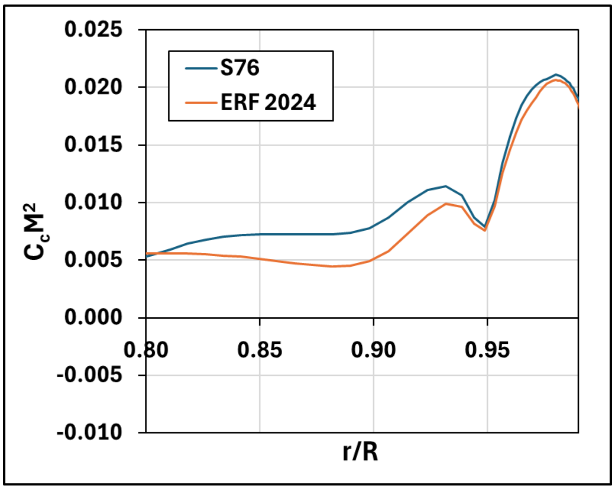

Figure 10: Radial variation of the Sectional Chordwise Force Coefficients C_cM^2 for the Two Rotors at 90% R

The radial variations of the sectional forces at this thrust setting have also been examined, as shown in Figure 9. There was negligible difference between the two rotors for the normal force coefficient, multiplied by the local section Mach number squared. This was expected since the two rotors have been trimmed to the same thrust setting. The chordwise force coefficients, again multiplied by the local Mach number squared, show more significant differences, as seen in Figure 10. The in-plane components of the normal force (acting as induced drag) and the chordwise force (contributing to profile drag) would therefore be lower for the new rotor. As a result, a modest reduction in power consumption, and a 1% improvement in figure of merit was achieved at this thrust setting (from 0.713 to 0.722). At higher settings, the improvement in the Figure of Merit was even more, as shown in Figure 7c.

5. CONCLUDING REMARKS

An inverse design method, previously developed by the present authors for aircraft components has been used to redesign rotorcraft SC 1095 airfoil section within a 2-D framework. This design process has also been used to redesign the tip region of the S76 rotor. Satisfactory improvements in the figure of merit, which translates into lower fuel consumption, have been achieved for a broad range of thrust settings.

Because the present design methodology is independent of the underlying aerodynamics analysis, and only relies on the predicted surface pressure data, this approach can be used with other flow solvers in use within academia, industry, and government. Additional work is needed to explore the potential of this approach for redesigning existing rotor geometries, and for the development of new families of blade sections and rotor configurations.

Author contact:

Michelle Ku mku7@gatech.edu

Aishwerya Gahlot aishwerya@gatech.edu

Lakshmi N. Sankar lsankar@ae.gatech.edu

6. REFERENCES

1. Johnson, W., "NDARC:NASA Design and Analysis of Rotorcraft Input," Volume 3, NASA/TP– 20220000355.
2. Johnson, W., "NDARC:NASA Design and Analysis of Rotorcraft Input and Data Structures," Volume 2, NASA/TP– 20220000355.
3. Johnson, W., "NDARC:NASA Design and Analysis of Rotorcraft Theory," Volume 1, NASA/TP– 20220000355.
4. Johnson, W., "A Quiet Helicopter for Air Taxi Operations" Presented at the VFS Aeromechanics for Advanced Vertical Flight Technical Meeting, San Jose, CA, January 21–23, 2020,
5. Silva, C., Johnson, W., "Practical Conceptual Design of Quieter Urban VTOL Aircraft," Presented at the Vertical Flight Society's 77th Annual Forum & Technology Display, Virtual, May 10–14, 2021.
6. Johnson, W. and Silva, C., "NASA Concept Vehicles and the Engineering of Advanced Air Mobility Aircraft," The Aeronautical Journal (2022), 126, pp. 59–91.
7. Johnson ,W. ,Elmore ,J. ,Keen , E., Gallaher, A., and Nunez ,G. ,"Coaxial Compound Helicopter for Confined Urban Operations," Presented at the AHS Specialists' Conference on Aeromechanics Design for Vertical Lift, San Francisco, CA, January 20-22, 2016.
8. K. Collins, L. Sankar, D. Mavris, "Application of Low- and High-Fidelity Simulation Tools to Helicopter Rotor Blade Optimization," Journal of the American Helicopter Society, Volume 58, No. 4, October 2013.
9. Garabedian ,P. and McFadden, G., "Design of Supercritical Swept Wings," AIAA Journal,Vol.20, No.3, 1982 , pp.289-291.
10. Jameson, Antony, Caughey, D. A., Newman, P. A., and Davis, R. M., "A Brief Description of the Jameson-Caughey NYU Transonic Swept-Wing Computer Program FLO-22; NASA TMX-73996, 1976.
11. Malone, J., Narramore, J. and Sankar, L. N., "An Efficient Airfoil Design Method Using the Navier-Stokes Equations," Proceedings of the AGARD Specialists Meeting on Computational Methods for Aerodynamic Design (inverse) and Optimization, Loen, Norway, May 22-23, 1989.
12. Malone ,J.B., Vadyak, J. and Sankar, L.N., "Inverse Aerodynamic Design Method for Aircraft Components," Journal of Aircraft, Vol. 24, No. 1, pp. 8-9, 1987.
13. Santos, L. and Sankar, L. N.,"A Hybrid Inverse Optimization method for the Aerodynamic Design of Lifting Surfaces," AIAA Paper 94-1895.
14. Sankar, L. N., Aerodynamics Notes, http://www.sankar.gatech.edu/sites/default/files/Panel.Methods.pdf, Georgia Institute of Technology, Atlanta, GA.
15. Sankar, L. N., 2-D Panel Code Script, http://www.sankar.gatech.edu/sites/default/files/2D_Panel.Code_.MATLAB.txt, Georgia Institute of Technology, Atlanta, GA.
16. AIAA HPW | Hover Prediction Workshop URL: https://www.aiaa-hpw.org/ .
17. Balch, D. T., "Experimental Study of Main Rotor Tip Geometry and Tail Rotor Interactions in

Hover, Volume 1, Test and Figures," NASA CR 177336, 1985.

18. Balch, D. T., "Experimental Study of Main Rotor Tip Geometry and Tail Rotor Interactions in Hover, Volume 2, Run Log and Tabulated Data," NASA CR 177336, 1985.

19. Marpu, R., Sankar, L. N., Egolf, A., Hariharan, N., "Analysis of a Rotor in Hover using Hybrid Methodology," AIAA Paper 2014-0210.

20. Zhou, C., Sankar, L. N. and Griffin, P., "Effects of Anhedral on S-76 Hover Aerodynamics," in AIAA SciTech Forum, San Diego, California, 2019.

21. Chen, Po-Wei, "A Physics Based Model for Inflow Characteristics of Multi-Rotor Configurations, " PhD Dissertation, Georgia Institute of Technology, August 2021.

22. Shankar, Shivani, Sankar, L. N., and Chen, Po-Wei, "Effects of Anhedral Tip on Hover Performance," AIAA SciTech Forum, January 2023.